

# Parity order as a fundamental driver of bosonic topology

Ashirbad Padhan  <sup>1,\*</sup> and Harsh Nigam  <sup>2,†</sup>

<sup>1</sup>Univ. Toulouse, CNRS, Laboratoire de Physique Théorique, Toulouse, France

<sup>2</sup>International Centre for Theoretical Sciences, Tata Institute of Fundamental Research, Bangalore 560089, India

(Dated: January 1, 2026)

Symmetry-protected topological (SPT) phases in interacting bosonic systems have been extensively studied, yet most realizations rely on fine-tuned interactions or enlarged symmetries. Here we show that a qualitatively different mechanism—parity order coupled to bond dimerization—acts as a fundamental driver of bosonic topology. Using density matrix renormalization group simulations, we identify two distinct topological phases absent in the purely dimerized model: an SPT phase at half filling stabilized by positive parity coupling, and a topological phase at unit filling stabilized by negative coupling that can be adiabatically connected to a trivial phase without breaking any symmetry. Our results establish parity order as a new organizing principle for correlation-driven bosonic topology.

**Introduction**— The recognition that phases of matter can be classified by topology, rather than by symmetry breaking alone, has profoundly reshaped our understanding of quantum systems. Topological phases exhibit robust properties such as quantized responses and protected boundary modes that remain stable against local perturbations [1, 2]. Originally crystallized in the context of the quantum Hall effect [3, 4], these ideas have since permeated condensed-matter and cold-atom physics, motivating the search for minimal lattice models in which topological mechanisms can be identified.

In one dimension, the Su–Schrieffer–Heeger (SSH) model [5, 6] provides the paradigmatic example. It describes fermions hopping on a dimerized chain and realizes a symmetry-protected topological (SPT) phase, distinguished from a trivial insulator by chiral and inversion symmetries and manifested through robust zero-energy edge states [7, 8]. Beyond its original realization in polyacetylene, the SSH model has been implemented across a wide range of platforms, including photonic lattices [9–13], cold atoms in optical superlattices [14–17], Rydberg-atom arrays [18], semiconductor nanolattices [19], momentum-space lattices [20, 21], mechanical systems [22], electrical circuits [23, 24], and superconducting qubits [25].

A natural question is how such topological features generalize beyond free fermions, particularly in bosonic systems where local constraints and correlations play a central role [26]. Interacting extensions of the SSH chain have been studied for spinless fermions and hardcore bosons, where Hubbard-type or nearest-neighbor interactions generate Mott phases, bond order phases, and interaction-driven transitions [19, 27–34]. On the bosonic side, the Haldane phase of integer-spin chains [35–54] provides the canonical interacting SPT phase, protected by discrete symmetries and characterized by nonlocal string order and edge states. Bosonic analogues of SSH-type models have been explored in this setting, showing that constraints or repulsive interactions can stabilize nontrivial topology even in the absence of fermionic statistics [28, 53, 55–58]. However, most lattice realizations of bosonic SPT phases rely on fine-tuned interactions or symmetry enrichment beyond minimal onsite U(1) or  $\mathbb{Z}_2$  symmetries, such as enlarged internal or crystalline spatial symmetries [59, 60]. As a result, the minimal route to

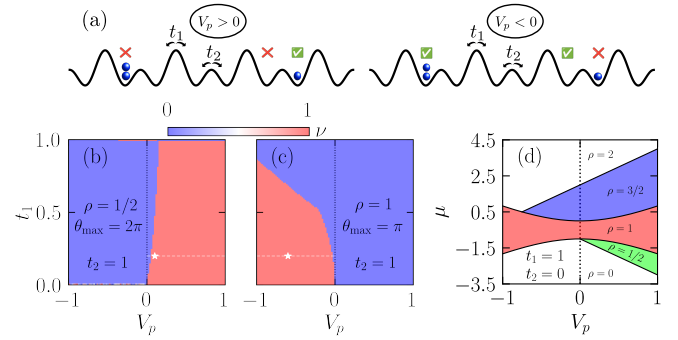


FIG. 1. (a) Schematic of the Hamiltonian in Eq. (1), describing bosons on a dimerized chain with an onsite parity coupling:  $V_p > 0$  ( $V_p < 0$ ) energetically favors odd (even) site occupations. (b) Twisted phase winding number  $\nu$  in the  $t_1$ - $V_p$  plane at half filling ( $\rho = 1/2$ ) for  $L = 8$  and  $t_2 = 1$ , showing a nontrivial phase with  $\nu = 1$  stabilized by positive parity coupling. The white star marks the BKT-type SF-BO transition point along the  $t_1 = 0.2$  cut. (c) Corresponding winding number at unit filling ( $\rho = 1$ ), where a topological phase is stabilized for  $V_p < 0$ . The white star indicates the crossover between BO and PBO phases along the  $t_1 = 0.2$  cut. (d) Phase diagram in the chemical potential  $\mu$ - $V_p$  plane in the isolated-dimer limit ( $t_1 = 1, t_2 = 0$ ), with phase boundaries obtained from Eq. (EM27), highlighting gapped phases at different fillings.

bosonic SPT phases in lattice systems remains unsettled, motivating the search for simpler organizing principles.

**Model**— In this Letter, we introduce a simple extension that achieves this goal: bosons on a dimerized chain with an additional onsite coupling to the local parity of the occupation, described by the Hamiltonian

$$\hat{H} = -t_1 \sum_{j \in \text{even}} (\hat{b}_j^\dagger \hat{b}_{j+1} + \text{H.c.}) - t_2 \sum_{j \in \text{odd}} (\hat{b}_j^\dagger \hat{b}_{j+1} + \text{H.c.}) + V_p \sum_j (-1)^{\hat{n}_j}, \quad (1)$$

where  $\hat{b}_j^{(\dagger)}$  annihilates (creates) a boson at site  $j$  and  $\hat{n}_j = \hat{b}_j^\dagger \hat{b}_j$ . The first two terms describe bosonic hopping with alternating amplitudes  $t_1$  and  $t_2$ , which reduce to the bosonic SSH chain in the absence of the parity coupling ( $V_p = 0$ ). The

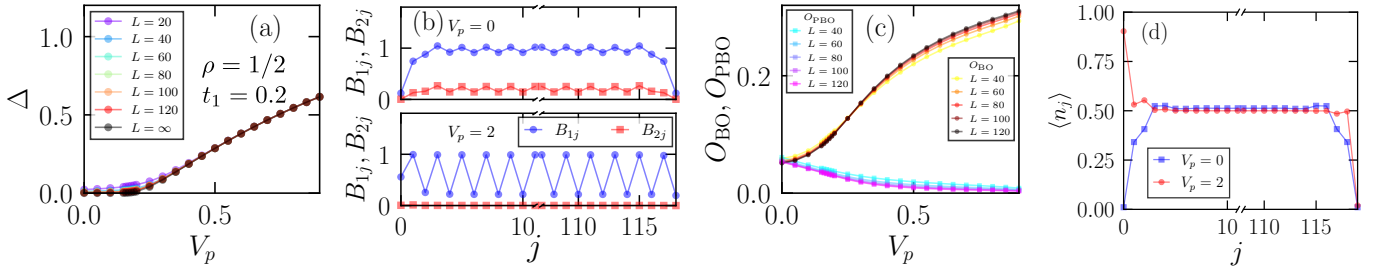


FIG. 2. Half filling ( $\rho = 1/2$ ) at  $t_1 = 0.2$ . (a) Charge gap under periodic boundary conditions as a function of  $V_p$  for  $L = 20, 40, 60, 80, 100, 120$ , together with an extrapolation to the thermodynamic limit, signaling a BKT-type superfluid–bond order transition. (b) Bond energies  $B_{1j}$  and  $B_{2j}$  as functions of the bond index  $j$  at  $V_p = 0$  (superfluid phase) and  $V_p = 2$  (bond order phase) for  $L = 120$ . (c) Bond order parameter  $O_{\text{BO}}$  and pair bond order parameter  $O_{\text{PBO}}$  as functions of  $V_p$  for  $L = 40, 60, 80, 100, 120$ . (d) Onsite densities  $\langle n_j \rangle$  at  $V_p = 0$  and  $V_p = 2$  for  $L = 120$ , illustrating the distinct density profiles associated with the bond order phase.

last term couples directly to the local occupation parity  $(-1)^{\hat{n}_j}$ , energetically favoring even or odd site occupations depending on the sign of  $V_p$  (see Fig. 1(a) and the two-boson, two-site analysis in Sec. EM2).

The Hamiltonian in Eq. (1) preserves an exact on-site  $\mathbb{Z}_2$  symmetry generated by the global parity operator  $\hat{P} = \prod_j (-1)^{\hat{n}_j}$ . The parity term commutes with  $\hat{P}$  and partitions the many-body Hilbert space into even- and odd-parity sectors, without introducing explicit density–density interactions.

We study this model using density matrix renormalization group simulations [61–64] in the canonical ensemble, primarily with open boundary conditions. Systems of up to  $L = 120$  sites are considered, keeping bond dimensions up to  $\chi = 800$  and discarding Schmidt values below  $10^{-10}$ . Unless stated otherwise, we set  $t_2 = 1$  as the energy unit and focus on the regime  $t_1 \leq t_2$  over a range of fillings  $\rho = N/L$ , where  $N$  is the total number of bosons. We impose a three-body constraint ( $n_{\text{max}} = 2$ ), restricting  $n_j = 0, 1, 2$  and yielding parity eigenvalues  $(+1, -1, +1)$ ; the key topological results at a given filling remain robust for  $n_{\text{max}} > 2$  (Sec. EM6). Within this constrained Hilbert space, the model maps onto an effective spin-1 Hamiltonian (Sec. EM1).

**Main results**— Our central result is that the parity coupling qualitatively reshapes the phase diagram of the dimerized bosonic chain. For positive  $V_p$ , a topological phase emerges at half filling ( $\rho = 1/2$ ), whereas for negative  $V_p$  a distinct topological phase is realized at unit filling ( $\rho = 1$ ). Both phases are absent in the purely dimerized limit ( $V_p = 0$ ), demonstrating that parity order, when combined with bond dimerization, provides a minimal mechanism for stabilizing bosonic topological phases in one dimension.

To characterize the bulk topology of these phases, we compute the twisted phase winding number,

$$\nu = \frac{1}{2\pi} \int_0^{\theta_{\text{max}}} d\theta \partial_\theta \arg \langle \Psi(\theta) | \Psi(\theta + \delta\theta) \rangle, \quad (2)$$

where  $|\Psi(\theta)\rangle$  denotes the many-body ground state satisfying the twisted boundary condition  $\hat{b}_{L+1} = e^{i\theta} \hat{b}_1$  [55, 56, 65, 66]. At half filling, the twist spans the full interval  $\theta_{\text{max}} = 2\pi$ . By contrast, at unit filling and for  $V_p < 0$ , boson pairing effec-

tively halves the Brillouin zone, resulting in  $\theta_{\text{max}} = \pi$  [56]. A quantized value  $\nu = 1$  signals a topological phase, while  $\nu = 0$  corresponds to a trivial one. We emphasize that a vanishing value of  $\nu$ , as defined here, does not distinguish between gapped and gapless phases.

We evaluate  $\nu$  using exact diagonalization on a small chain, which allows for explicit tracking of the Berry phase evolution under twisted boundary conditions. Figs. 1(b) and 1(c) display the resulting winding number in the  $V_p$ – $t_1$  plane at half and unit filling, respectively. At half filling [Fig. 1(b)], a topological phase with  $\nu = 1$  appears exclusively for positive parity coupling  $V_p > 0$ , stabilized by the interplay of bond dimerization and parity-induced even–odd occupation structure. At unit filling [Fig. 1(c)], the situation is inverted: the topological phase is realized only for negative coupling  $V_p < 0$ . In both cases, the topological region expands as the dimerization is strengthened, i.e., as  $t_1 \rightarrow 0$ .

Further insight into the origin of these phases is obtained from the isolated-dimer limit ( $t_1 \neq 0, t_2 = 0$ ). In this limit, the lattice decomposes into isolated dimers, and the phase structure can be understood from a simple two-site analysis (see Sec. EM3 for details). Fig. 1(d) shows the chemical potentials  $\mu$  as functions of  $V_p$ , with phase boundaries determined from Eq. (EM27) for  $t_1 = 1$ . The resulting phase diagram exhibits gapped phases at fillings  $\rho = 1/2, 1$ , and  $3/2$ . At half filling, a gap opens immediately for any  $V_p > 0$ , while at unit filling the system remains gapped even at  $V_p = 0$ , with the gap increasing on either side. A gapped phase is also observed at  $\rho = 3/2$ , which is dual to the one at  $\rho = 1/2$ ; here the gap opens for moderately negative parity coupling,  $V_p > -0.75$ . Together, this analysis confirms that the topological phases with  $\nu = 1$  at  $\rho = 1/2$  and  $\rho = 1$  are indeed gapped. Below, we focus on the topology at half and unit filling; details of the  $\rho = 3/2$  case are presented in Sec. EM5.

**Topology at half filling**— We first consider the half-filled regime, where the winding-number analysis indicates that a positive parity coupling stabilizes a topological phase. To further characterize this phase and the associated transition, we fix the dimerization strength to  $t_1 = 0.2$  [dashed cut in Fig. 1(b)] and increase  $V_p$  into the positive regime.

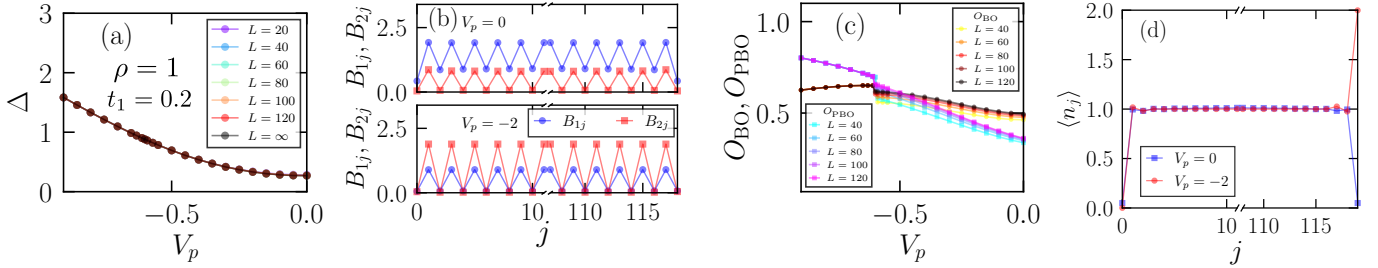


FIG. 3. Unit filling ( $\rho = 1$ ) at  $t_1 = 0.2$ . (a) Charge gap under periodic boundary conditions as a function of  $V_p$  for  $L = 20, 40, 60, 80, 100, 120$ , together with an extrapolation to the thermodynamic limit, showing that the gap remains finite throughout. (b) Bond energies  $B_{1j}$  and  $B_{2j}$  as functions of the bond index  $j$  at  $V_p = 0$  (bond order phase) and  $V_p = -2$  (pair bond order phase) for  $L = 120$ . (c) Bond order parameter  $O_{\text{BO}}$  and pair bond order parameter  $O_{\text{PBO}}$  as functions of  $V_p$  for  $L = 40, 60, 80, 100, 120$ . (d) Onsite densities  $\langle n_j \rangle$  at  $V_p = 0$  and  $V_p = -2$  for  $L = 120$ , highlighting the distinct density profiles associated with the pair bond order phase.

As a first proxy for the phase transition, we examine the charge gap,

$$\Delta = E_{N+1} + E_{N-1} - 2E_N, \quad (3)$$

where  $E_N$  denotes the ground-state energy with  $N$  bosons. Fig. 2(a) shows  $\Delta$ , extrapolated to the thermodynamic limit, as a function of  $V_p$  under periodic boundary conditions. At  $V_p = 0$ , the gap vanishes, consistent with a gapless superfluid (SF) phase. Upon increasing  $V_p$ , a finite gap opens for  $V_p \gtrsim 0.1$ , signaling a Berezinskii–Kosterlitz–Thouless (BKT)-type transition into a gapped phase (see Sec. EM8 for BKT scaling analysis).

To identify the nature of the gapless and gapped regimes, we compute the single- and two-particle bond energies,

$$B_{n,j} = \left\langle \left( \hat{b}_j^\dagger \right)^n \left( \hat{b}_{j+1} \right)^n + \text{H.c.} \right\rangle, \quad n = 1, 2, \quad (4)$$

shown in Fig. 2(b) as functions of the bond index  $j$  at the gapless point  $V_p = 0$  and deep in the gapped regime at  $V_p = 2$ . At  $V_p = 0$ , the single-particle contribution dominates, with  $B_{1,j} \sim 1$  and  $B_{2,j} \approx 0$ , and exhibits only weak spatial modulation in the bulk. In contrast, at  $V_p = 2$ ,  $B_{1,j}$  displays pronounced oscillations characteristic of bond dimerization, while  $B_{2,j}$  remains negligible. These features identify the gapped phase as a bond order (BO) phase.

To quantitatively characterize this ordering, we define the bond order (BO) and pair bond order (PBO) parameters as

$$O_{\text{BO(PBO)}} = \frac{1}{L-1} \sum_j (-1)^j B_{1(2),j}, \quad (5)$$

respectively. Fig. 2(c) shows  $O_{\text{BO}}$  and  $O_{\text{PBO}}$  as functions of  $V_p$ , obtained by averaging over the bulk region ( $j \in [L/4, 3L/4 - 1]$ ).  $O_{\text{BO}}$  decreases with increasing system size in the SF phase and grows in the BO phase, exhibiting a crossing at  $V_p \sim 0.2$ , slightly larger than the critical value inferred from the charge gap. By contrast,  $O_{\text{PBO}}$  vanishes with increasing  $L$  throughout, ruling out the formation of a paired phase. Taken together, these results establish a BKT-type SF–BO transition at  $\rho = 1/2$  occurring at  $V_p \sim 0.1$  [marked by the white star in Fig. 1(b)].

While the bulk properties reveal that the gapped phase is a BO phase, a direct manifestation of its topology appears in the local density profile, particularly near the boundaries. Fig. 2(d) compares the on-site density  $\langle n_j \rangle$  for  $V_p = 0$  and  $V_p = 2$ . At  $V_p = 0$ , the density is uniform throughout the lattice,  $\langle n_j \rangle \sim 1.0$ , with small edge deviations attributable to Friedel oscillations. In contrast, at  $V_p = 2$ , the bulk density remains uniform at  $\langle n_j \rangle \sim 1.0$ , but a pronounced imbalance develops at the edges: one edge is occupied ( $\langle n_j \rangle \sim 1.0$ ), while the other is nearly empty ( $\langle n_j \rangle \sim 0.0$ ). This asymmetric edge density provides a clear real-space signature of the nontrivial topology of the BO phase.

*Topology at unit filling*— We now turn to the unit-filled regime, where the winding-number analysis indicates that a distinct topological phase is stabilized by negative parity coupling. To analyze this case, we again fix the dimerization strength to  $t_1 = 0.2$  [dashed cut in Fig. 1(c)] and decrease  $V_p$  into the negative regime.

As in the half-filled case, the charge gap provides the first indication of the nature of the phases [Fig. 3(a)]. Here,  $\Delta$  remains finite throughout and increases smoothly as  $V_p$  becomes more negative. Notably, the gap does not close at  $V_p = 0$ , even in the thermodynamic limit. This behavior follows from the isolated-dimer picture discussed earlier (see Fig. 1(d) and Sec. EM3), which shows that the unit-filled system remains gapped for all values of  $V_p$ .

To characterize the bulk ordering, Fig. 3(b) shows the site-resolved single- and two-particle bond energies  $B_{1j}$  and  $B_{2j}$  at  $V_p = 0$  and deep in the gapped regime at  $V_p = -2$ . At  $V_p = 0$ , both bond energies exhibit spatial oscillations; however,  $B_{1j}$  dominates over  $B_{2j}$  on all bonds. This identifies the phase at  $V_p = 0$  as a BO phase, consistent with the presence of a finite charge gap. In contrast, at strong negative parity coupling ( $V_p = -2$ ), both  $B_{1j}$  and  $B_{2j}$  exhibit spatial oscillations; however,  $B_{2j}$  becomes the dominant contribution. It displays pronounced dimerized oscillations, alternating between nearly vanishing and large values on adjacent bonds, while  $B_{1j}$  remains smaller throughout. This behavior signals the formation of bound boson pairs that coherently tunnel between neighboring sites with alternating amplitudes. We therefore identify

this regime as a PBO phase.

To further substantiate the bond-energy oscillations, Fig. 3(c) shows  $O_{\text{BO}}$  and  $O_{\text{PBO}}$ , obtained by averaging over the bulk region, as functions of  $V_p$  for several system sizes. At  $V_p = 0$ ,  $O_{\text{BO}}$  clearly dominates and increases with system size, while  $O_{\text{PBO}}$  also grows but remains parametrically smaller, consistent with the identification of a BO phase. As  $V_p$  is tuned towards negative values, both order parameters increase and cross near  $V_p \simeq -0.6$ . Beyond this point,  $O_{\text{PBO}}$  becomes the dominant contribution and continues to grow, while  $O_{\text{BO}}$  decreases as the negative parity coupling is further strengthened. This behavior signals a smooth crossover from the BO phase to the PBO phase at  $V_p \simeq -0.6$  [marked by the white star in Fig. 1(c)], indicating that the two phases are adiabatically connected without a closing of the bulk gap. Notably, both order parameters exhibit a sharp change in magnitude near the crossover, reflecting a rapid reorganization of the dominant bond correlations rather than a true quantum phase transition.

Topological features of these phases are revealed most directly through the local density profile, as shown in Fig. 3(d). In the BO regime ( $V_p = 0$ ), the density remains uniform in the bulk at  $\langle n_j \rangle \sim 1.0$ , with small deviations near the boundaries attributable to Friedel oscillations. In contrast, in the PBO regime ( $V_p = -2$ ), while the bulk density remains uniform at unit filling, a pronounced density imbalance emerges at the edges, with one boundary hosting  $\langle n_j \rangle \sim 2.0$  and the opposite boundary nearly empty. This boundary-localized density asymmetry provides a clear real-space signature of the non-trivial topology of the PBO phase.

*Decoding the topology*— The distinct topological behaviors at half and unit fillings can be traced back to their effective low-energy descriptions derived in Sec. EM4. At  $\rho = 1/2$ , a positive parity coupling  $V_p > 0$  suppresses double occupancy and projects the system onto a hard-core boson manifold, yielding the effective dimerized Hamiltonian in Eq. (EM29). This model is adiabatically equivalent to the SSH chain and realizes a BO phase protected by bond-centered inversion symmetry. As long as inversion symmetry is preserved, the topological phase cannot be smoothly connected to another gapped phase without closing the bulk gap.

In contrast, at  $\rho = 1$ , negative parity coupling  $V_p < 0$  favors even site occupations and leads to an effective pair-hopping description, Eq. (EM32), corresponding to mobile boson pairs on a dimerized lattice. Although this regime supports a topological PBO phase, the smooth crossover between the BO and PBO regimes as a function of  $V_p$  indicates that this topology is not symmetry protected in general. Nevertheless, in the large- $|V_p|$  limit the effective pair-hopping model inherits a chiral (sublattice) symmetry analogous to that of the SSH model, providing a natural explanation for the emergence of topological features in this regime despite their adiabatic connection to a trivial phase.

*Insights from the local parity operator*— To gain further intuition into the parity-driven mechanisms underlying the phases discussed above (along the  $t_1 = 0.2$  cut), we intro-

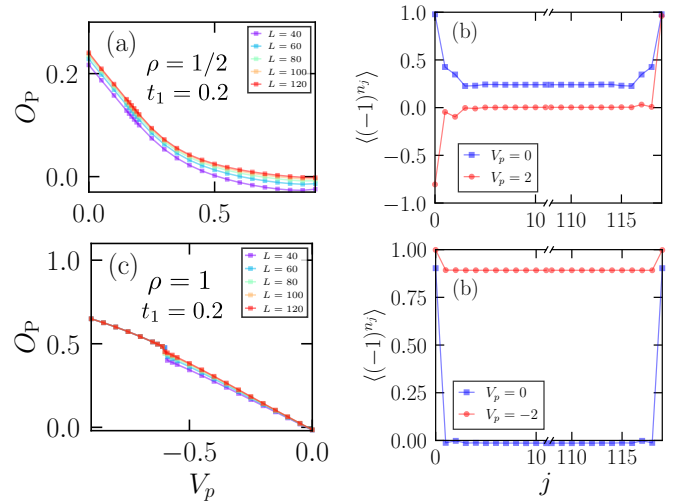


FIG. 4. Results for  $t_1 = 0.2$ . (a) Parity order parameter  $O_P$  as a function of  $V_p$  at half filling ( $\rho = 1/2$ ), decreasing from a finite value in the superfluid phase to zero upon entering the bond order phase. (b) Site-resolved expectation value of the parity operator  $\langle (-1)^{\hat{n}_j} \rangle$  for  $V_p = 0$  and  $V_p = 2$  at  $\rho = 1/2$  for  $L = 120$ . (c) Parity order parameter  $O_P$  at unit filling ( $\rho = 1$ ), decreasing from a large value in the pair bond order phase toward zero in the bond order phase. (d) Site-resolved expectation value of the parity operator  $\langle (-1)^{\hat{n}_j} \rangle$  for  $V_p = 0$  and  $V_p = -2$  at  $\rho = 1/2$  for  $L = 120$ .

duce a simple local diagnostic: the spatially averaged parity expectation value

$$O_P = \frac{1}{L} \sum_j \langle (-1)^{\hat{n}_j} \rangle, \quad (6)$$

which directly probes the imbalance between even and odd onsite occupations and, as discussed in Sec. EM7, admits a transparent analytical interpretation across different phases and fillings in terms of local occupation probabilities.

Figs. 4(a) and (b) show  $O_P$ —with averaging performed over the bulk region—together with the site-resolved parity  $\langle (-1)^{\hat{n}_j} \rangle$  at  $\rho = 1/2$ . As shown in Fig. 4(a),  $O_P$  decreases from a finite value in the SF phase to zero in the BO phase as  $V_p$  increases. The real-space profiles in Fig. 4(b) corroborate this picture: the bulk parity remains finite and nearly uniform at  $V_p = 0$  (SF phase), whereas at  $V_p = 2$  (BO phase) the bulk parity vanishes and the two edges exhibit opposite parity, consistent with the edge-state signatures in Fig. 2(d).

A qualitatively different behavior emerges at  $\rho = 1$ , as shown in Figs. 4(c) and (d). Here,  $O_P$  evolves smoothly from a vanishing value to positive values as  $V_p$  is tuned from zero toward negative values, with a sharp change near  $V_p \simeq -0.6$  marking the BO–PBO crossover. The corresponding site-resolved profiles show that, while the bulk parity remains vanishingly small at  $V_p = 0$  (BO phase), it becomes large and positive at  $V_p = -2$  (PBO phase), including at the edges. This behavior signals the dominance of even occupations associated with boson pairing and is consistent with the edge-state signatures in Fig. 3(d).

*Summary and outlook*— In summary, we have shown that nontrivial bosonic topology can emerge without explicit density–density interactions or the need for enlarged protecting symmetries, arising instead from the interplay between a local occupation parity coupling  $V_p$  and bond dimerization. The parity term reshapes the low-energy Hilbert space and, when combined with dimerized hopping, gives rise to distinct topological responses at different commensurate fillings.

At half filling, the system realizes a topological bond order (BO) phase protected by bond-centered inversion symmetry, which cannot be adiabatically connected to a trivial gapped phase without breaking this symmetry. This protection can be explicitly lifted, for example, by introducing an inversion-breaking staggered sublattice potential. By contrast, at unit filling the smooth crossover between the BO and pair bond order (PBO) regimes indicates that the corresponding topology is not symmetry protected, even though the large- $|V_p|$  limit admits an effective SSH-like description.

Notably, the topological features show close correspondence with earlier studies of SSH models with Bose–Hubbard interactions. While the half-filled case was identified in Ref. [55], the unit-filling behavior parallels that reported in Ref. [56]. This correspondence is particularly striking here, since positive  $V_p$  penalizes even empty occupations, underscoring a fundamentally different microscopic route to topology.

The parity coupling  $V_p$  considered here has previously been discussed in a different context [67], indicating that the present model is physical rather than merely a mathematical construction. It would be particularly interesting to identify realizations in quantum simulation platforms such as ultracold atoms in optical lattices [68–73], where local occupation parity and dimerized tunneling can be engineered and controlled.

Finally, while Figs. 1(b) and 1(c) provide an overview of the phase structure, a systematic determination of phase boundaries separating gapped and gapless regimes is left for future work. It will also be interesting to explore whether global parity can protect the topology in this setting, and how such protection may be selectively broken, for example by introducing pair- or correlated-hopping processes. More broadly, our work opens new directions for engineering bosonic quantum phases by tailoring local constraints rather than conventional interactions.

*Acknowledgments*— We thank Ankush Chaubey and Krushna Chandra Sahu for carefully reading the manuscript. A.P. acknowledges NISER Bhubaneswar for hospitality during a visit where the first results of this work were obtained. H.N. acknowledges support from the Department of Atomic Energy, Government of India, under Project No. RTI4001. This research was supported in part by the International Centre for Theoretical Sciences (ICTS) through the discussion meeting \*10th Indian Statistical Physics Community Meeting\* (Code: ICTS/ISPCM2025/04), where the collaboration leading to this work was initiated.

## End Matter

### EM1. MAPPING TO AN EFFECTIVE SPIN-1 HAMILTONIAN

Our bosonic model in Eq. (1), subject to the three-body constraint  $n_j = 0, 1, 2$ , can be mapped to an effective spin-1 chain [37].

We can map the bosonic operators onto spin-1 operators via

$$\hat{n}_j = S_j^z + 1, \quad \hat{b}_j = \frac{1}{\sqrt{2}}(1 + S_j^z)S_j^-, \quad \hat{b}_j^\dagger = \frac{1}{\sqrt{2}}S_j^+(1 + S_j^z). \quad (\text{EM1})$$

This identification corresponds to  $|0\rangle \leftrightarrow |S_j^z = -1\rangle$ ,  $|1\rangle \leftrightarrow |S_j^z = 0\rangle$ , and  $|2\rangle \leftrightarrow |S_j^z = +1\rangle$ .

Using Eq. (EM1), the parity operator becomes

$$(-1)^{\hat{n}_j} = 2(S_j^z)^2 - 1, \quad (\text{EM2})$$

so that the parity coupling maps exactly to a single-ion anisotropy,

$$V_p \sum_j (-1)^{\hat{n}_j} = 2V_p \sum_j (S_j^z)^2 - V_p L. \quad (\text{EM3})$$

Projecting the hopping terms yields an alternating XY exchange,

$$-t_j(\hat{b}_j^\dagger \hat{b}_{j+1} + \text{H.c.}) \rightarrow J_j(S_j^x S_{j+1}^x + S_j^y S_{j+1}^y), \quad (\text{EM4})$$

with  $J_j \propto t_j$  inheriting the bond dimerization.

The resulting effective spin-1 Hamiltonian is therefore

$$\hat{H}_{\text{eff}} = \sum_j J_j(S_j^x S_{j+1}^x + S_j^y S_{j+1}^y) + 2V_p \sum_j (S_j^z)^2 - V_p L. \quad (\text{EM5})$$

At half filling and  $V_p > 0$ , the low-energy sector involves  $S_j^z = 0, -1$ , yielding an effective dimerized spin-1/2 chain with symmetry-protected topology. At unit filling and large negative  $V_p$ , the low-energy manifold reduces to  $S_j^z = \pm 1$ , corresponding to mobile boson pairs and a topological phase.

### EM2. TWO-SITE DESCRIPTION AT UNIT FILLING WITHOUT DIMERIZATION

We consider the minimal realization of the parity model on two lattice sites with two bosons in total (unit filling) and without dimerization, i.e.,  $t_1 = t_2 = t$ . The Hamiltonian reads

$$\hat{H} = -t \left( \hat{b}_0^\dagger \hat{b}_1 + \hat{b}_1^\dagger \hat{b}_0 \right) + V_p \left[ (-1)^{\hat{n}_0} + (-1)^{\hat{n}_1} \right]. \quad (\text{EM6})$$

At fixed particle number  $N = 2$ , the allowed Fock basis is

$$\{|2, 0\rangle, |1, 1\rangle, |0, 2\rangle\}, \quad (\text{EM7})$$

where  $|n_0, n_1\rangle$  denotes the occupation of sites  $j = 0, 1$ . In this basis, the Hamiltonian takes the matrix form

$$H = \begin{pmatrix} 2V_p & -\sqrt{2}t & 0 \\ -\sqrt{2}t & -2V_p & -\sqrt{2}t \\ 0 & -\sqrt{2}t & 2V_p \end{pmatrix}. \quad (\text{EM8})$$

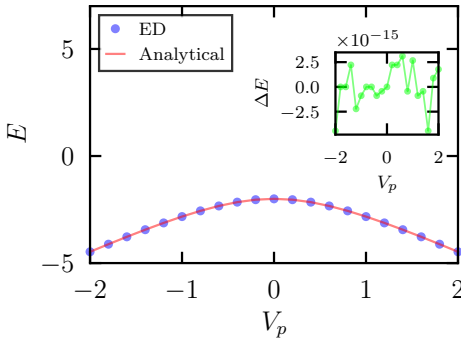


FIG. EM1. Ground-state energy of the two-site model at unit filling with  $t_1 = t_2 = t = 1$  as a function of the parity coupling  $V_p$ . Symbols show exact diagonalization (ED) results, while the solid line corresponds to the analytical expression in Eq. (EM14). The inset displays the difference between numerical and analytical energies.

Introducing symmetric and antisymmetric pair states,

$$|S\rangle = \frac{1}{\sqrt{2}} (|2, 0\rangle + |0, 2\rangle), \quad (\text{EM9})$$

$$|A\rangle = \frac{1}{\sqrt{2}} (|2, 0\rangle - |0, 2\rangle), \quad (\text{EM10})$$

the antisymmetric state  $|A\rangle$  is an exact eigenstate with energy  $E_A = 2V_p$  and remains uncoupled from the singly occupied configuration  $|1, 1\rangle$ .

As a result, the Hamiltonian block-diagonalizes, and the nontrivial physics is entirely captured by the symmetric subspace spanned by  $\{|S\rangle, |1, 1\rangle\}$ . In this basis, the Hamiltonian reduces to

$$H_{\text{sym}} = \begin{pmatrix} 2V_p & -2t \\ -2t & -2V_p \end{pmatrix}, \quad (\text{EM11})$$

with eigenvalues

$$E_{\pm} = \pm 2\sqrt{V_p^2 + t^2}. \quad (\text{EM12})$$

The ground-state wave function can be written explicitly as

$$|\Psi\rangle = \frac{1}{\sqrt{2\sqrt{V_p^2 + t^2}}} \left[ \sqrt{\sqrt{V_p^2 + t^2} + V_p} |1, 1\rangle - \sqrt{\sqrt{V_p^2 + t^2} - V_p} |S\rangle \right], \quad (\text{EM13})$$

with ground-state energy

$$E = -2\sqrt{V_p^2 + t^2}. \quad (\text{EM14})$$

For  $V_p \gg t$ , the parity potential dominates over hopping and the ground state approaches the singly occupied configuration  $|1, 1\rangle$ , which maximizes odd parity on each site. The system

thus realizes an odd-parity Mott-like state in which particle-number fluctuations are strongly suppressed.

In contrast, for  $-V_p \gg t$ , even parity is energetically favored and the ground state approaches the symmetric pair state  $(|2, 0\rangle + |0, 2\rangle)/\sqrt{2}$ , corresponding to complete delocalization of a boson pair across the two sites.

At  $V_p = 0$ , the parity term vanishes and the ground state is an equal-weight superposition of the singly occupied and symmetric pair configurations, reflecting maximal hybridization between single-particle and pair degrees of freedom driven solely by hopping.

For completeness, Fig. EM1 compares the ground-state energy obtained from exact diagonalization of Eq. (EM8) with the analytical expression in Eq. (EM14), showing excellent agreement.

### EM3. ISOLATED-DIMER LIMIT ANALYSIS

In the isolated-dimer limit  $t_2 = 0$ , the system decomposes into independent two-site unit cells. The Hamiltonian in Eq. (1) for a single unit cell becomes

$$\hat{H}_{\text{cell}} = -t_1 (\hat{b}_0^\dagger \hat{b}_1 + \hat{b}_1^\dagger \hat{b}_0) + V_p [(-1)^{\hat{n}_0} + (-1)^{\hat{n}_1}]. \quad (\text{EM15})$$

Using the same analysis provided in Sec. EM2 at different fillings  $\rho = N/2$ , we lead to the following results.

#### A. $\rho = 0$ ( $N = 0$ )

The ground state is the vacuum

$$|\psi_0\rangle = |00\rangle, \quad (\text{EM16})$$

with energy

$$E_0 = 2V_p. \quad (\text{EM17})$$

Both sites are even occupied, and the energy is entirely set by the parity term.

#### B. $\rho = 1/2$ ( $N = 1$ )

The single-particle ground state is a symmetric delocalized state,

$$|\psi_{1/2}\rangle = \frac{1}{\sqrt{2}} (|10\rangle + |01\rangle), \quad (\text{EM18})$$

with energy

$$E_1 = -t_1. \quad (\text{EM19})$$

The parity contributions cancel between the two sites, and the energy gain arises solely from kinetic delocalization within the unit cell, producing a BO phase.

### C. $\rho = 1 (N = 2)$

The ground state is a superposition of singly and doubly occupied configurations,

$$|\psi_1\rangle = \alpha (|20\rangle + |02\rangle) + \beta |11\rangle, \quad (\text{EM20})$$

with ground-state energy

$$E_2 = -2\sqrt{V_p^2 + t_1^2}, \quad (\text{EM21})$$

which is same as in Eq. (EM14) with  $t_1 = t$ . For  $V_p > 0$ , odd occupation is favored and  $\beta \rightarrow 1$ , yielding a Mott-like state  $|11\rangle$ . For  $V_p < 0$ , even occupation is favored and  $\alpha \rightarrow 1/\sqrt{2}$ , corresponding to a PBO state.

### D. $\rho = 3/2 (N = 3)$

The three-particle ground state is

$$|\psi_{3/2}\rangle = \frac{1}{\sqrt{2}} (|21\rangle + |12\rangle), \quad (\text{EM22})$$

with energy

$$E_3 = -2t_1. \quad (\text{EM23})$$

Parity contributions again cancel, and the kinetic term delocalizes the composite object within the unit cell, leading to a higher-filling BO phase.

### E. $\rho = 2 (N = 4)$

The fully occupied ground state is

$$|\psi_2\rangle = |22\rangle, \quad (\text{EM24})$$

with energy

$$E_4 = 2V_p. \quad (\text{EM25})$$

This state is purely parity dominated and has no kinetic contribution.

## F. Chemical potentials

Chemical potentials are obtained from finite differences,

$$\mu_N = E_{N+1} - E_N, \quad (\text{EM26})$$

yielding

$$\begin{aligned} \mu_0 &= -t_1 - 2V_p, \\ \mu_1 &= -\sqrt{4V_p^2 + 4t_1^2} + t_1, \\ \mu_2 &= -2t_1 + \sqrt{4V_p^2 + 4t_1^2}, \\ \mu_3 &= 2V_p + 2t_1. \end{aligned} \quad (\text{EM27})$$

## EM4. EFFECTIVE MODELS FOR PARITY-DRIVEN TOPOLOGY

### A. Half filling ( $\rho = 1/2$ )

For  $V_p > 0$ , odd on-site occupations are energetically favored, while parity fluctuations are separated by an energy scale set by  $V_p$ . At  $\rho = 1/2$  and for  $V_p \gg t_{1,2}$ , the low-energy Hilbert space is therefore restricted to at most one boson per site,

$$\mathcal{H}_{\text{low}}^{(1/2)} = \{n_j = 0, 1\}. \quad (\text{EM28})$$

Projecting the full Hamiltonian onto  $\mathcal{H}_{\text{low}}^{(1/2)}$ ,  $\hat{H}_{\text{eff}} = \mathcal{P} \hat{H} \mathcal{P}$  with  $\mathcal{P}$  the corresponding projector, yields

$$\hat{H}_{\text{eff}}^{(1/2)} = - \sum_j t_j \left( \hat{c}_j^\dagger \hat{c}_{j+1} + \text{H.c.} \right) + \text{const.}, \quad (\text{EM29})$$

where  $\hat{c}_j^{(\dagger)}$  are hard-core boson operators obeying  $(\hat{c}_j^\dagger)^2 = 0$ , and  $t_j = t_1, t_2$  on alternating bonds.

Eq. (EM29) describes a dimerized hard-core boson chain, which is equivalent via a Jordan–Wigner transformation [74] to the fermionic SSH model [5], thereby explaining the emergence of an SPT BO phase.

### B. Unit filling ( $\rho = 1$ )

For  $V_p < 0$ , even on-site occupations are favored. At  $\rho = 1$  and for  $|V_p| \gg t_{1,2}$ , the low-energy sector is dominated by doubly occupied sites,

$$\mathcal{H}_{\text{low}}^{(1)} = \{n_j = 2\}, \quad (\text{EM30})$$

while singly occupied configurations are separated by an energy gap of order  $|V_p|$ .

Single-particle hopping is therefore suppressed and contributes only virtually. To second order in  $t_{1,2}/|V_p|$ , a Schrieffer–Wolff transformation [75] generates effective pair-hopping processes,

$$\hat{H}_{\text{eff}}^{(1)} = \bar{\mathcal{P}} \left( \hat{H}_t \frac{1}{E_0 - \hat{H}_p} \hat{H}_t \right) \bar{\mathcal{P}}, \quad (\text{EM31})$$

where  $\hat{H}_t$  and  $\hat{H}_p$  denote the hopping and parity terms of Eq. (1), respectively and  $\bar{\mathcal{P}}$  is projector to  $\mathcal{H}_{\text{low}}^{(1)}$ . Evaluating this expression yields

$$\hat{H}_{\text{eff}}^{(1)} = - \sum_j t_j^{(2)} \left( \hat{d}_j^\dagger \hat{d}_{j+1} + \text{H.c.} \right) + \text{const.}, \quad (\text{EM32})$$

with  $\hat{d}_j^\dagger \equiv (\hat{b}_j^\dagger)^2$  creating a boson pair and  $t_j^{(2)} \sim t_j^2/|V_p|$ .

Eq. (EM32) describes boson pairs hopping on a dimerized lattice and explains the emergence of the topological PBO phase.

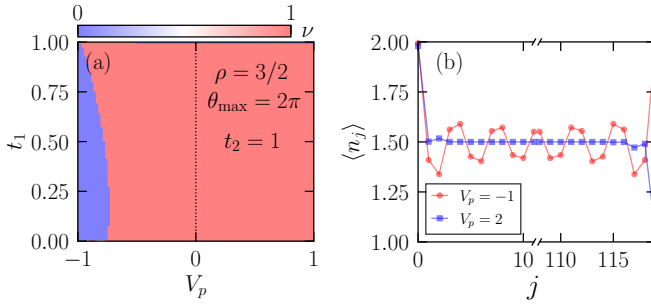


FIG. EM2. Topological properties at filling  $\rho = 3/2$ , dual to those at  $\rho = 1/2$ . (a) Twisted phase winding number  $\nu$  in the  $t_1$ – $V_p$  plane for  $L = 8$  and  $t_2 = 1$ , showing that the topological regime extends into the region  $V_p < 0$ . (b) Site-resolved density  $\langle n_j \rangle$  along  $t_1 = 0.2$  cut at  $V_p = -1$  and  $V_p = 2$  for  $L = 120$ .

### EM5. TOPOLOGICAL PHASE AT FILLING $\rho = 3/2$

This section demonstrates that the gapped phase at filling  $\rho = 3/2$  is also topological in nature. Fig. EM2(a) shows the twisted phase winding number  $\nu$  computed using ED as a function of  $V_p$  and  $t_1$  at  $\rho = 3/2$ . In contrast to the half-filled case ( $\rho = 1/2$ ), the topological region now extends into the  $V_p < 0$  regime, consistent with the behavior observed in Fig. 1(d). This reflects the duality between the gapped phases at fillings  $\rho$  and  $2 - \rho$ .

Direct real-space signatures of this topology are shown in Fig. EM2(b). For  $V_p = -1.0$ , the density profile is featureless, and no edge localization is observed, consistent with a trivial phase. In contrast, for  $V_p = 2$ , clear edge-state signatures emerge: the bulk density remains uniform at  $\langle n_j \rangle \simeq 1.5$ , while one edge site is preferentially occupied with density  $\langle n_j \rangle \simeq 2$ , and the opposite edge is depleted to  $\langle n_j \rangle \simeq 1$ . This asymmetric edge occupation provides direct real-space evidence for the topological nature of the gapped phase at  $\rho = 3/2$ .

### EM6. ROBUSTNESS BEYOND THE THREE-BODY CONSTRAINT

Here we assess the stability of the half-filled topological phase upon relaxing the three-body constraint. Fig. EM3 shows the site-resolved density  $\langle n_j \rangle$  for several local occupation cutoffs  $n_{\max} > 2$ , with parameters  $t_1 = 0.2$  and  $V_p = 2$ .

For all values of  $n_{\max}$  considered, the bulk density remains uniform at  $\langle n_j \rangle \simeq 0.5$ . At the same time, a pronounced density imbalance persists at the boundaries, with one edge hosting excess occupation and the opposite edge being depleted. This robust edge-state signature demonstrates that the half-filled topological phase does not rely on the three-body constraint and remains stable when higher on-site occupancies are allowed.

By contrast, the topological features observed at  $\rho = 1$  and  $\rho = 3/2$  are unstable beyond the three-body constraint and disappear upon increasing  $n_{\max}$  (not shown).

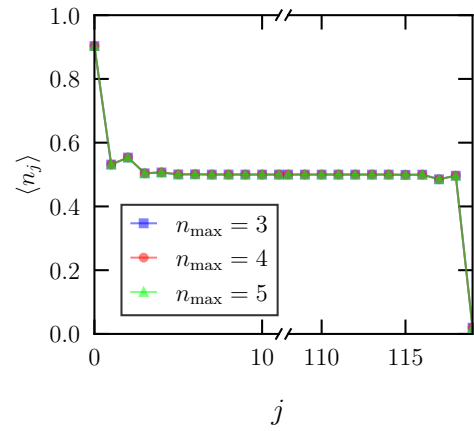


FIG. EM3. Site-resolved density  $\langle n_j \rangle$  at half filling ( $\rho = 1/2$ ) for different local occupation cutoffs  $n_{\max} > 2$  on a chain of length  $L = 120$ , with parameters  $t_1 = 0.2$  and  $V_p = 2$ . The bulk density remains uniform at  $\langle n_j \rangle \simeq 0.5$ , while a persistent edge density imbalance signals the presence of topological boundary modes beyond the three-body constraint.

### EM7. LOCAL PARITY EXPECTATION VALUE IN DIFFERENT PHASES ACROSS FILLINGS

Here we analyze the local parity operator

$$\hat{P}_j = (-1)^{\hat{n}_j}, \quad (\text{EM33})$$

which measures the imbalance between even and odd onsite occupancies. For a general local occupation distribution  $P_j(n)$ ,

$$\langle \hat{P}_j \rangle = \sum_{n=0}^{\infty} (-1)^n P_j(n) = P_{\text{even}} - P_{\text{odd}}. \quad (\text{EM34})$$

#### A. Insulating phases

In the isolated-dimer limit,  $\langle \hat{P}_j \rangle$  can be obtained analytically for all commensurate fillings.

At  $\rho = 0$  and  $\rho = 2$ , the ground state is a trivial product state with strictly even occupation on every site, yielding

$$\langle \hat{P}_j \rangle = +1. \quad (\text{EM35})$$

At half-integer fillings  $\rho = \frac{1}{2}$  and  $\rho = \frac{3}{2}$ , the ground state is bond ordered, with particles delocalized within each unit cell. The local occupation probabilities satisfy  $P_{\text{even}} = P_{\text{odd}} = 1/2$ , giving

$$\langle \hat{P}_j \rangle = 0, \quad (\text{EM36})$$

demonstrating that parity does not detect bond order.

At unit filling  $\rho = 1$ , the parity expectation value sharply distinguishes the Mott insulator (MI) and the PBO phase. The dimer ground state can be written as

$$|\psi\rangle = \alpha(|20\rangle + |02\rangle) + \beta|11\rangle, \quad (\text{EM37})$$

leading to

$$\langle \hat{P}_j \rangle = 1 - 2\beta^2 = \frac{V_p}{\sqrt{V_p^2 + t_1^2}}. \quad (\text{EM38})$$

Consequently,  $\langle \hat{P}_j \rangle = -1$  in the MI phase ( $V_p > 0$ ) and  $+1$  in the PBO phase ( $V_p < 0$ ), with a continuous sign change at  $V_p = 0$ .

## B. Superfluid regime at different fillings

In compressible regions between insulating plateaus, the system enters a superfluid (SF) phase characterized by strong number fluctuations. Approximating the local state by a coherent state with mean density  $\bar{n} = \langle \hat{n}_j \rangle$ , the onsite occupation follows approximately a Poisson distribution, yielding the universal expression

$$\langle \hat{P}_j \rangle_{\text{SF}} = \sum_{n=0}^{\infty} (-1)^n e^{-\bar{n}} \frac{\bar{n}^n}{n!} = e^{-2\bar{n}}. \quad (\text{EM39})$$

This result implies a smooth, filling-dependent parity expectation:

$$\langle \hat{P}_j \rangle_{\text{SF}} \simeq \begin{cases} 1, & \rho \ll 1, \\ e^{-1}, & \rho = \frac{1}{2}, \\ e^{-2}, & \rho = 1, \\ e^{-3}, & \rho = \frac{3}{2}, \\ 0, & \rho \gg 1, \end{cases} \quad (\text{EM40})$$

Thus, unlike insulating phases, the SF exhibits a finite but non-quantized parity expectation that decays exponentially with increasing density.

The local parity expectation value provides a unified characterization across all fillings: it is quantized in insulating phases, vanishes in bond order phases, and assumes smooth, filling-dependent values in the superfluid. In particular,  $\langle \hat{P}_j \rangle$  acts as a local order parameter distinguishing the MI and PBO phases at unit filling.

## EM8. BEREZINSKII-KOSTERLITZ-THOULESS (BKT) SCALING ANALYSIS

Here we investigate the SF-BO phase transition at half filling as a function of  $V_p$ . For  $V_p < V_c$  the system is SF and gapless, whereas for  $V_p > V_c$  it exhibits a gapped BO phase. The transition is therefore expected to belong to the Berezinskii-Kosterlitz-Thouless (BKT) universality class [76–78]. From the scaling analysis discussed below, we determine the critical coupling to be  $V_c = 0.1$ .

To characterize the transition, we analyze the finite-size scaling of the charge gap  $\Delta(L, V_p)$ . On the gapped side of a

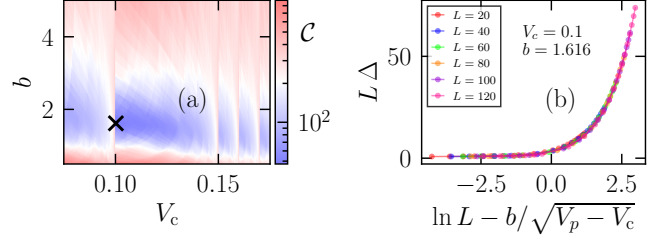


FIG. EM4. (a) Cost-function landscape  $C$  obtained from the BKT scaling collapse of the charge gap, shown as a function of the trial parameters  $V_c$  and  $b$ . The cross marks the global minimum, yielding  $V_c = 0.1$  and  $b = 1.616$ . (b) Scaling collapse of  $L\Delta(L, V_p)$  plotted against the BKT scaling variable  $\ln L - b / \sqrt{V_p - V_c}$ , using the optimal parameters extracted from panel (a).

BKT transition, the gap exhibits an essential singularity,

$$\Delta(V_p) \sim \exp\left[-\frac{b}{\sqrt{V_p - V_c}}\right], \quad V_p > V_c, \quad (\text{EM41})$$

where  $b$  is a nonuniversal constant. This form implies a rapidly diverging correlation length  $\xi \sim \exp[b/\sqrt{V_p - V_c}]$ , which controls the finite-size dependence near criticality.

Guided by this behavior, we perform a minimal BKT scaling collapse using the scaling variables

$$x = \ln L - \frac{b}{\sqrt{V_p - V_c}}, \quad y = L\Delta(L, V_p), \quad (\text{EM42})$$

retaining only data on the gapped side  $V_p > V_c$ . For the correct choice of  $V_c$  and  $b$ , data obtained for different system sizes collapse onto a single universal curve.

The optimal parameters are determined by minimizing a collapse cost function  $C$ , defined as follows. All data points are binned according to the scaling variable  $x$  into intervals of width  $\delta x$ . Within each bin  $k$ , we compute the variance of the scaled gap  $y$ ,

$$\sigma_k^2 = \frac{1}{N_k} \sum_{i \in k} (y_i - \bar{y}_k)^2, \quad (\text{EM43})$$

where  $N_k$  is the number of points in bin  $k$  and  $\bar{y}_k$  is the bin average. The total cost function is then defined as

$$C(V_c, b) = \sum_k \sigma_k^2, \quad (\text{EM44})$$

which quantitatively measures the quality of the data collapse.

Fig. EM4 illustrates this procedure. In Fig. EM4(a), we show the cost-function landscape  $C(V_c, b)$ , which displays a well-defined minimum at  $V_c = 0.1$  and  $b = 1.616$ . Using these values, Fig. EM4(b) demonstrates an excellent collapse of  $L\Delta$  for all system sizes considered, providing strong numerical evidence that the SF-BO transition at half filling is governed by BKT criticality.

\* ashirbad.padhan@irsamc.ups-tlse.fr  
 † harsh.nigam@icts.res.in

[1] M. Z. Hasan and C. L. Kane, Colloquium: Topological insulators, *Rev. Mod. Phys.* **82**, 3045 (2010).

[2] X.-L. Qi and S.-C. Zhang, Topological insulators and superconductors, *Rev. Mod. Phys.* **83**, 1057 (2011).

[3] R. B. Laughlin, Quantized hall conductivity in two dimensions, *Phys. Rev. B* **23**, 5632 (1981).

[4] D. J. Thouless, M. Kohmoto, M. P. Nightingale, and M. den Nijs, Quantized hall conductance in a two-dimensional periodic potential, *Phys. Rev. Lett.* **49**, 405 (1982).

[5] W. P. Su, J. R. Schrieffer, and A. J. Heeger, Solitons in polyacetylene, *Phys. Rev. Lett.* **42**, 1698 (1979).

[6] W. P. Su, J. R. Schrieffer, and A. J. Heeger, Soliton excitations in polyacetylene, *Phys. Rev. B* **22**, 2099 (1980).

[7] J. K. Asbóth, L. Oroszlány, and A. Pályi, *A Short Course on Topological Insulators* (Springer International Publishing, 2016).

[8] S. Ryu, A. P. Schnyder, A. Furusaki, and A. W. W. Ludwig, Topological insulators and superconductors: tenfold way and dimensional hierarchy, *New Journal of Physics* **12**, 065010 (2010).

[9] R. Keil, J. M. Zeuner, F. Dreisow, M. Heinrich, A. Tünnermann, S. Nolte, and A. Szameit, The random mass dirac model and long-range correlations on an integrated optical platform, *Nature Communications* **4**, 1368 (2013).

[10] M. Xiao, Z. Q. Zhang, and C. T. Chan, Surface impedance and bulk band geometric phases in one-dimensional systems, *Phys. Rev. X* **4**, 021017 (2014).

[11] F. Cardano, A. D'Errico, A. Dauphin, M. Maffei, B. Piccirillo, C. de Lisio, G. De Filippis, V. Cataudella, E. Santamato, L. Marzucci, M. Lewenstein, and P. Massignan, Detection of zak phases and topological invariants in a chiral quantum walk of twisted photons, *Nature Communications* **8**, 10.1038/ncomms15516 (2017).

[12] T. Kitagawa, M. A. Broome, A. Fedrizzi, M. S. Rudner, E. Berg, I. Kassal, A. Aspuru-Guzik, E. Demler, and A. G. White, Observation of topologically protected bound states in photonic quantum walks, *Nature Communications* **3**, 10.1038/ncomms1872 (2012).

[13] C. Jörg, M. Jürgensen, S. Mukherjee, and M. C. Rechtsman, Optical control of topological end states via soliton formation in a 1d lattice, *Nanophotonics* **14**, 769–775 (2024).

[14] M. Atala, M. Aidelsburger, J. T. Barreiro, D. Abanin, T. Kitagawa, E. Demler, and I. Bloch, Direct measurement of the zak phase in topological bloch bands, *Nature Physics* **9**, 795–800 (2013).

[15] M. Lohse, C. Schweizer, O. Zilberberg, M. Aidelsburger, and I. Bloch, A thouless quantum pump with ultracold bosonic atoms in an optical superlattice, *Nature Physics* **12**, 350–354 (2015).

[16] S. Nakajima, T. Tomita, S. Taie, T. Ichinose, H. Ozawa, L. Wang, M. Troyer, and Y. Takahashi, Topological thouless pumping of ultracold fermions, *Nature Physics* **12**, 296–300 (2016).

[17] M. Leder, C. Grossert, L. Sitta, M. Genske, A. Rosch, and M. Weitz, Real-space imaging of a topologically protected edge state with ultracold atoms in an amplitude-chirped optical lattice, *Nature Communications* **7**, 10.1038/ncomms13112 (2016).

[18] S. de Léséleuc, V. Lienhard, P. Scholl, D. Barredo, S. Weber, N. Lang, H. P. Büchler, T. Lahaye, and A. Browaeys, Observation of a symmetry-protected topological phase of interacting bosons with rydberg atoms, *Science* **365**, 775–780 (2019).

[19] N. H. Le, A. J. Fisher, N. J. Curson, and E. Ginossar, Topological phases of a dimerized fermi–hubbard model for semiconductor nano-lattices, *npj Quantum Information* **6**, 10.1038/s41534-020-0253-9 (2020).

[20] E. J. Meier, F. A. An, and B. Gadway, Observation of the topological soliton state in the su–schrieffer–heeger model, *Nature Communications* **7**, 10.1038/ncomms13986 (2016).

[21] D. Xie, W. Gou, T. Xiao, B. Gadway, and B. Yan, Topological characterizations of an extended su–schrieffer–heeger model, *npj Quantum Information* **5**, 10.1038/s41534-019-0159-6 (2019).

[22] L. Thatcher, P. Fairfield, L. Merlo-Ramírez, and J. M. Merlo, Experimental observation of topological phase transitions in a mechanical 1d-ssh model, *Physica Scripta* **97**, 035702 (2022).

[23] Y. Liu, W. Cao, W. Chen, H. Wang, L. Yang, and X. Zhang, Fully integrated topological electronics, *Scientific Reports* **12**, 13410 (2022).

[24] C. H. Lee, S. Imhof, C. Berger, F. Bayer, J. Brehm, L. W. Molenkamp, T. Kiessling, and R. Thomale, Topoelectrical circuits, *Communications Physics* **1**, 39 (2018).

[25] Y. Liu, Y.-R. Zhang, Y.-H. Shi, T. Liu, C. Lu, Y.-Y. Wang, H. Li, T.-M. Li, C.-L. Deng, S.-Y. Zhou, T. Liu, J.-C. Zhang, G.-H. Liang, Z.-Y. Mei, W.-G. Ma, H.-T. Liu, Z.-H. Liu, C.-T. Chen, K. Huang, X. Song, S. P. Zhao, Y. Tian, Z. Xiang, D. Zheng, F. Nori, K. Xu, and H. Fan, Interplay between disorder and topology in thouless pumping on a superconducting quantum processor, *Nature Communications* **16**, 10.1038/s41467-024-55343-2 (2025).

[26] S. Rachel, Interacting topological insulators: a review, *Reports on Progress in Physics* **81**, 116501 (2018).

[27] H. Nigam, A. Padhan, D. Sen, T. Mishra, and S. Bhattacharjee, Phases and phase transitions in a dimerized spin- $\frac{1}{2}$  xxz chain, *Phys. Rev. B* **111**, 195131 (2025).

[28] A. Hayashi, S. Mondal, T. Mishra, and B. P. Das, Competing insulating phases in a dimerized extended bose-hubbard model, *Phys. Rev. A* **106**, 013313 (2022).

[29] F. Grusdt, M. Höning, and M. Fleischhauer, Topological edge states in the one-dimensional superlattice bose-hubbard model, *Phys. Rev. Lett.* **110**, 260405 (2013).

[30] M. Di Liberto, A. Recati, I. Carusotto, and C. Menotti, Two-body physics in the su–schrieffer–heeger model, *Phys. Rev. A* **94**, 062704 (2016).

[31] X. Zhou, J.-S. Pan, and S. Jia, Exploring interacting topological insulator in the extended su–schrieffer–heeger model, *Phys. Rev. B* **107**, 054105 (2023).

[32] S. Mondal, S. Greschner, L. Santos, and T. Mishra, Topological inheritance in two-component hubbard models with single-component su–schrieffer–heeger dimerization, *Phys. Rev. A* **104**, 013315 (2021).

[33] X. Zhou, J.-S. Pan, and S. Jia, Exploring interacting topological insulator in the extended su–schrieffer–heeger model, *Phys. Rev. B* **107**, 054105 (2023).

[34] A. Padhan, S. Mondal, S. Vishveshwara, and T. Mishra, Interacting bosons on a su–schrieffer–heeger ladder: Topological phases and thouless pumping, *Phys. Rev. B* **109**, 085120 (2024).

[35] F. D. M. Haldane, Nonlinear field theory of large-spin heisenberg antiferromagnets: Semiclassically quantized solitons of the one-dimensional easy-axis néel state, *Phys. Rev. Lett.* **50**, 1153 (1983).

[36] I. Affleck, T. Kennedy, E. H. Lieb, and H. Tasaki, Rigorous results on valence-bond ground states in antiferromagnets, *Phys. Rev. Lett.* **59**, 799 (1987).

[37] E. G. Dalla Torre, E. Berg, and E. Altman, Hidden order in 1d bose insulators, *Phys. Rev. Lett.* **97**, 260401 (2006).

[38] E. Berg, E. G. Dalla Torre, T. Giamarchi, and E. Altman, Rise

and fall of hidden string order of lattice bosons, *Phys. Rev. B* **77**, 245119 (2008).

[39] H. Nonne, P. Lecheminant, S. Capponi, G. Roux, and E. Boulat, Haldane charge conjecture in one-dimensional multicomponent fermionic cold atoms, *Phys. Rev. B* **81**, 020408 (2010).

[40] M. Dalmonte, M. Di Dio, L. Barbiero, and F. Ortolani, Homogeneous and inhomogeneous magnetic phases of constrained dipolar bosons, *Phys. Rev. B* **83**, 155110 (2011).

[41] X. Deng and L. Santos, Entanglement spectrum of one-dimensional extended bose-hubbard models, *Phys. Rev. B* **84**, 085138 (2011).

[42] S. Furukawa, M. Sato, S. Onoda, and A. Furusaki, Ground-state phase diagram of a spin- $\frac{1}{2}$  frustrated ferromagnetic xxz chain: Haldane dimer phase and gapped/gapless chiral phases, *Phys. Rev. B* **86**, 094417 (2012).

[43] D. Rossini and R. Fazio, Phase diagram of the extended bose-hubbard model, *New Journal of Physics* **14**, 065012 (2012).

[44] K. Kobayashi, M. Okumura, Y. Ota, S. Yamada, and M. Machida, Nontrivial haldane phase of an atomic two-component fermi gas trapped in a 1d optical lattice, *Phys. Rev. Lett.* **109**, 235302 (2012).

[45] E. G. D. Torre, Dynamical probing of a topological phase of bosons in one dimension, *Journal of Physics B: Atomic, Molecular and Optical Physics* **46**, 085303 (2013).

[46] L. Barbiero, A. Montorsi, and M. Roncaglia, How hidden orders generate gaps in one-dimensional fermionic systems, *Phys. Rev. B* **88**, 035109 (2013).

[47] S. Ejima and H. Fehske, Comparative density-matrix renormalization group study of symmetry-protected topological phases in spin-1 chain and bose-hubbard models, *Phys. Rev. B* **91**, 045121 (2015).

[48] S. Fazzini, A. Montorsi, M. Roncaglia, and L. Barbiero, Hidden magnetism in periodically modulated one dimensional dipolar fermions, *New Journal of Physics* **19**, 123008 (2017).

[49] L. Barbiero, L. Dell'Anna, A. Trombettoni, and V. E. Korepin, Haldane topological orders in motzkin spin chains, *Phys. Rev. B* **96**, 180404 (2017).

[50] K. Kottmann, P. Huembeli, M. Lewenstein, and A. Acín, Unsupervised phase discovery with deep anomaly detection, *Phys. Rev. Lett.* **125**, 170603 (2020).

[51] B. Hetényi, Interaction-driven polarization shift in the  $t-v-V'$  lattice fermion model at half filling: Emergent haldane phase, *Phys. Rev. Res.* **2**, 023277 (2020).

[52] K. Kottmann, A. Haller, A. Acín, G. E. Astrakharchik, and M. Lewenstein, Supersolid-superfluid phase separation in the extended bose-hubbard model, *Phys. Rev. B* **104**, 174514 (2021).

[53] J. Fraxanet, D. González-Cuadra, T. Pfau, M. Lewenstein, T. Langen, and L. Barbiero, Topological quantum critical points in the extended bose-hubbard model, *Phys. Rev. Lett.* **128**, 043402 (2022).

[54] M. Łącki, H. Korbmacher, G. A. Domínguez-Castro, J. Zajączkowski, and L. Santos, Ground states of one-dimensional dipolar lattice bosons at unit filling, *Phys. Rev. B* **109**, 125104 (2024).

[55] F. Grusdt, M. Höning, and M. Fleischhauer, Topological edge states in the one-dimensional superlattice bose-hubbard model, *Phys. Rev. Lett.* **110**, 260405 (2013).

[56] S. Greschner, S. Mondal, and T. Mishra, Topological charge pumping of bound bosonic pairs, *Phys. Rev. A* **101**, 053630 (2020).

[57] K. Sugimoto, S. Ejima, F. Lange, and H. Fehske, Quantum phase transitions in the dimerized extended bose-hubbard model, *Phys. Rev. A* **99**, 012122 (2019).

[58] D. Wellnitz, G. A. Domínguez-Castro, T. Bilitewski, M. Aidelsburger, A. M. Rey, and L. Santos, Emergent interaction-induced topology in bose-hubbard ladders, *Phys. Rev. Res.* **7**, L012012 (2025).

[59] Y. You, T. Devakul, F. J. Burnell, and T. Neupert, Higher-order symmetry-protected topological states for interacting bosons and fermions, *Phys. Rev. B* **98**, 235102 (2018).

[60] A. Rasmussen and Y.-M. Lu, Classification and construction of higher-order symmetry-protected topological phases of interacting bosons, *Phys. Rev. B* **101**, 085137 (2020).

[61] S. R. White, Density matrix formulation for quantum renormalization groups, *Phys. Rev. Lett.* **69**, 2863 (1992).

[62] S. R. White, Density-matrix algorithms for quantum renormalization groups, *Phys. Rev. B* **48**, 10345 (1993).

[63] U. Schollwöck, The density-matrix renormalization group in the age of matrix product states, *Annals of Physics* **326**, 96 (2011), january 2011 Special Issue.

[64] N. Nakatani, Matrix product states and density matrix renormalization group algorithm, in *Reference Module in Chemistry, Molecular Sciences and Chemical Engineering* (Elsevier, 2018).

[65] Y. Hatsugai, Quantized berry phases as a local order parameter of a quantum liquid, *Journal of the Physical Society of Japan* **75**, 123601 (2006).

[66] Y. Hatsugai, Quantized berry phases for a local characterization of spin liquids in frustrated spin systems, *Journal of Physics: Condensed Matter* **19**, 145209 (2007).

[67] K. Sun and C. J. Bolech, Bose-hubbard model with occupation-parity couplings, *Phys. Rev. B* **89**, 064506 (2014).

[68] F. Schäfer, T. Fukuhara, S. Sugawa, Y. Takasu, and Y. Takahashi, Tools for quantum simulation with ultracold atoms in optical lattices, *Nature Reviews Physics* **2**, 411–425 (2020).

[69] C. Gross and I. Bloch, Quantum simulations with ultracold atoms in optical lattices, *Science* **357**, 995 (2017).

[70] I. Bloch, J. Dalibard, and S. Nascimbène, Quantum simulations with ultracold quantum gases, *Nature Physics* **8**, 267 (2012).

[71] M. Lewenstein, A. Sanpera, V. Ahufinger, B. Damski, A. Sen(De), and U. Sen, Ultracold atomic gases in optical lattices: mimicking condensed matter physics and beyond, *Advances in Physics* **56**, 243 (2007), <https://doi.org/10.1080/00018730701223200>.

[72] I. Bloch, J. Dalibard, and W. Zwerger, Many-body physics with ultracold gases, *Rev. Mod. Phys.* **80**, 885 (2008).

[73] M. Lewenstein, A. Sanpera, and V. Ahufinger, *Ultracold Atoms in Optical Lattices: Simulating quantum many-body systems* (Oxford University Press, 2012).

[74] P. Jordan and E. Wigner, Über das paulische äquivalenzverbot, *Zeitschrift für Physik* **47**, 631 (1928).

[75] A. Auerbach, *Interacting Electrons and Quantum Magnetism* (Springer New York, 1994).

[76] V. L. Berezinskii, Destruction of Long-range Order in One-dimensional and Two-dimensional Systems having a Continuous Symmetry Group I. Classical Systems, *Soviet Journal of Experimental and Theoretical Physics* **32**, 493 (1971).

[77] J. M. Kosterlitz and D. J. Thouless, Ordering, metastability and phase transitions in two-dimensional systems, *Journal of Physics C: Solid State Physics* **6**, 1181 (1973).

[78] M. A. Cazalilla, R. Citro, T. Giamarchi, E. Orignac, and M. Rigol, One dimensional bosons: From condensed matter systems to ultracold gases, *Rev. Mod. Phys.* **83**, 1405 (2011).